

Small Y Addition Effects on Hot Deformation Behavior of Copper-Matrix Alloys

Yi Zhang,* Huili Sun,* Alex A. Volinsky, Bingjie Wang, Baohong Tian, Zhe Chai, Yong Liu, and Kexing Song

Hot deformation behavior of two alloys, Cu–Zr and Cu–Zr–Y is studied by compression tests using the Gleeble-1500D thermo-mechanical simulator. Experiments are conducted at 550–900 °C temperature and 0.001–10 s⁻¹ strain rate. The true stress–true strain curves are analyzed, and the results show that the flow stress strongly depends on the temperature and the strain rate. Furthermore, both alloys behave similarly when the flow stress increases with higher strain rate and lower temperature. Based on the dynamic material model, the processing maps are obtained at strains of 0.4 and 0.5. The optimal processing parameters for the Cu–Zr and Cu–Zr–Y alloys are determined. In addition, the constitutive equations for the alloys are established to characterize the flow stress as a function of strain rate and deformation temperature. Based on the microstructure evolution analysis, the results show that the addition of Y can effectively promote dynamic recrystallization. Moreover, the processability of the alloy can be optimized. Thermal deformation activation energy and the peak power dissipation efficiency for the alloys are obtained. It is observed that the addition of Y effectively improves thermal deformation activation energy and has considerable influence on the peak power dissipation efficiency.

lead frame,^[6] and so on. Cu alloys with better mechanical properties are in high demand. Thus, many studies have been performed to improve the properties of Cu alloys. Hot extrusion and other plastic deformation processes, as well as solution and aging treatments, have always been regarded as excellent methods to significantly improve material mechanical properties by increasing dislocation density. In the past decade, there has been an influx of investigations in this area. Nevertheless, the above methods have shown little effect on electrical conductivity.^[7,8] Batra et al.^[9] reported that the addition of zirconium (Zr) could decrease the stacking fault energy of a copper matrix. Hence, the movement of dislocations can be greatly hindered, which improves the strength of Cu alloys.^[7] Ye et al.^[10] obtained the Cu–0.5Zr–0.065B (wt%) alloy by using a double deformation aging process with 575.4 MPa tensile strength and 79.37% IACS electrical conductivity. Zhang et al.^[11] researched the aging behavior of the Cu–0.4Cr–0.15Zr–0.05Ce (wt%) alloy and obtained a hardness

1. Introduction

Copper (Cu) alloys have recently been attracting more attention in terms of their high-temperature deformation behavior, excellent conductivity, and high strength.^[1–3] Due to their excellent performance, these materials are widely used as diverter target materials,^[4] contact wires,^[5] resistance welding,^[2]

of 183 HV with electrical conductivity reaching up to 83% IACS. Xia et al.^[12] pointed out that a combination of low electrical resistivity and high strength of the Cu–0.39Cr–0.24Zr–0.072Mg–0.021Si (wt%) alloy can be achieved after hot-rolling, quenching, and suitable thermo-mechanical treatment. In general, this Cu–Zr alloy has high strength, high softening temperature, and perfect wear performance.^[13,14]


Rare earth (RE) metals play an important role in the study of functional materials. As “the vitamin of modern industry”, RE containing alloys usually perform at exceedingly higher levels.^[15] REs can efficiently increase the purity of the alloy matrix due to the special physical capabilities and high chemical reactivity of free radicals.^[16–18]

Studies of Cu–Y alloys have been reported rarely, and the information mainly focused on powder metallurgy with Y content exceeding 0.8 wt%.^[19] Tan et al. obtained Cu–20Y (wt%) alloy by mechanical alloying, and concluded that the addition of Y can increase microhardness by grain size refinement.^[20] There are some researchers^[21] reporting that rare earth can decrease the stacking fault energy (SFE) of the alloy by enlarging the width of the extended dislocations. Pei et al.^[22] evaluated the effect of Y on the SFE in Mg by the Langmuir-McLean model and found

Dr. Y. Zhang, Dr. H. Sun, Dr. B. Wang,
Dr. B. Tian, Dr. Z. Chai, Dr. Y. Liu, Dr. K. Song
School of Materials Science and Engineering,
Henan University of Science and Technology,
Luoyang 471003, China

Collaborative Innovation Center of Nonferrous
Metals, Henan Province, Luoyang 471003, China
E-mail: zhshgu436@163.com; shllt0909@126.com;
volinsky@usf.edu

Dr. A. A. Volinsky
Department of Mechanical Engineering,
University of South Florida, Tampa 33620, USA

 The ORCID identification number(s) for the author(s) of this article can be found under <https://doi.org/10.1002/adem.201700197>.

DOI: 10.1002/adem.201700197

Table 1. Nominal and actual chemical components of the studied alloys (mass fraction, %).

Alloy	Zr		Y		Cu
	nominal	actual	nominal	actual	
Cu–Zr	0.2	0.147	0	0	Bal.
Cu–Zr–Y	0.2	0.192	0.15	0.138	Bal.

that the addition of Y can decrease the SFE. Meanwhile, there has been a focus on ternary or other multicomponent RE-containing Cu alloys. Zhang et al. added cerium (Ce) and concluded that it can improve deformation resistance and peak stress during hot deformation.^[23] However, these studies are limited to aging precipitation behavior, and very few literature reports of the RE studies focus on hot deformation behavior.

The present work studied hot deformation behavior of the Cu–0.2%Zr and Cu–0.2%Zr–0.15%Y alloys using the Gleeble-1500 simulator. The effects of a small addition of yttrium (Y) on the processing maps and microstructure were also studied. Comparison of constitutive equations and hot deformation activation energy (Q) for the two alloys are also reported.

2. Experimental Section

The two alloys deformed in this study were Cu–Zr and Cu–Zr–Y. They were fabricated in a vacuum induction furnace. Commercially pure Cu (99.99%), Zr (99.95%), and Y (99.95%) were used to prepare these alloys, which were then cast into a low carbon steel mold with $\Phi 83 \times 200$ mm dimensions. The smelting temperature was 1200–1250 °C with argon used as the protective gas. **Table 1** shows the nominal and actual chemical components, which were measured with inductively coupled plasma-optical emission spectrometry (ICP-OES).

Before deformation, the ingots were extruded to 33 mm diameter bars. Then, the bars were homogenized through solution heat treatment at 900 °C for 1 h, which almost dissolved the eutectic structure into the matrix. The maximum solubility of Zr in Cu at eutectic temperature is 0.15 wt%.^[24] The cylindrical specimen size used for hot deformation experiments was $\Phi 8 \times 12$ mm.

Hot deformation tests were performed using the Gleeble-1500D thermo-mechanical simulator with total deformation set to 55%. The experimental temperatures were 550, 650, 750, 850, and 900 °C, and the strain rates were 0.001, 0.01, 0.1, 1, and 10 s⁻¹. Before deformation, the temperature was increased to 1000 °C at a rate of 20 °C s⁻¹. To ensure uniform temperature distribution, this temperature was held for 6 min. When the temperature declined to the required set value, deformation was initiated at the different strain rates. To minimize the effects of friction, graphite tantalum sheets were

placed at the ends of the cylindrical samples. After deformation, the samples were immediately quenched in water to retain the thermoplastic deformation microstructure. The procedure for hot deformation is shown in **Figure 1a**. An OLYMPUS PMG3 optical microscope was used to observe microstructure evolution, and the solution structures for Cu–Zr and Cu–Zr–Y alloys are shown in **Figure 1b** and **c**. Metallographic samples were prepared by polishing and etching with a solution containing HCl + C₂H₅OH + FeCl₃. The precipitates were observed by a JEM-2100 high resolution transmission electron microscope (HRTEM). To prepare the samples for TEM, thin pieces were first cut from the compressed cylindrical sample parallel to the compressed direction, with the center parts chosen for TEM and diffraction observations. These were then thinned with an electrolyte of HNO₃ (20 ml) + C₂H₅OH (80 ml) in a DJ2000 twin-jet electropolisher. Finally, the samples were prepared by ion milling in a Gatan 691 ion beam thinner.

3. Results and Discussion

3.1. Flow Stress Behavior

Figure 2 shows true stress-true strain curves for the Cu–Zr and Cu–Zr–Y alloys obtained at different hot compression conditions. It can be clearly seen that the stress, strain, and deformation temperature are related. The flow stress for the two alloys decreases with temperature. The peak stress–temperature and peak stress–strain rate dependencies are shown in **Figure 3**. By increasing the strain rate, the peak stress of the two alloys

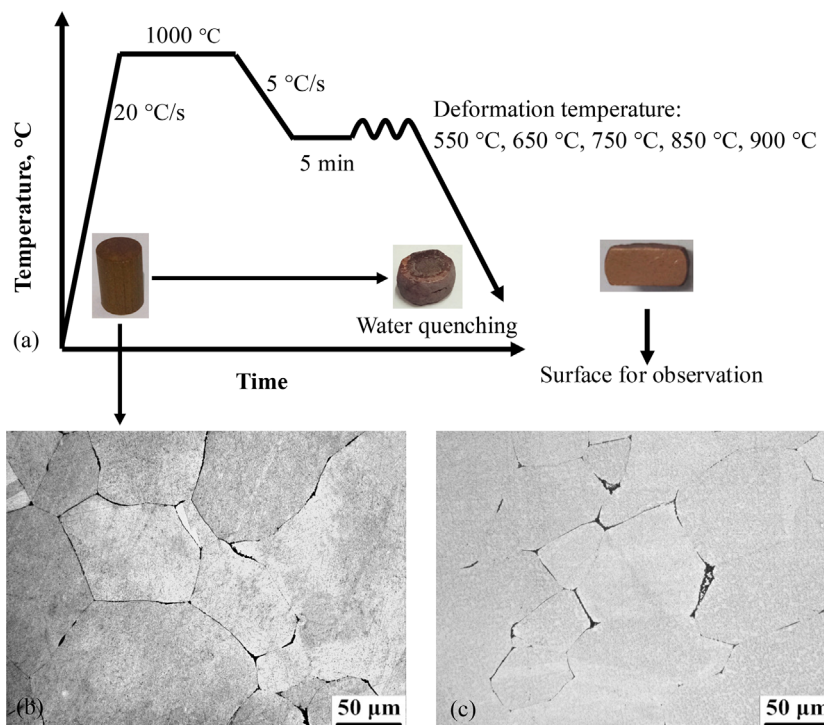


Figure 1. a) Experimental procedure for hot deformation and the solution structures for: b) Cu–Zr and c) Cu–Zr–Y alloys.

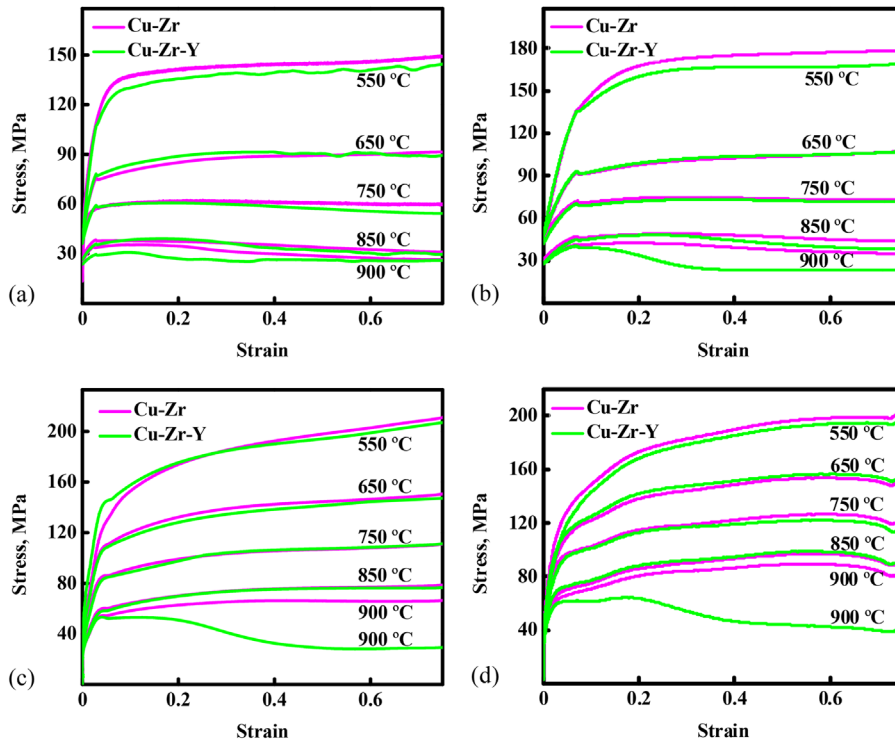


Figure 2. True stress–true strain curves of the Cu–Zr and Cu–Zr–Y alloys under different strain rates: a) 0.001 s^{-1} ; b) 0.01 s^{-1} ; c) 1 s^{-1} ; and d) 10 s^{-1} .

noticeably increased. Similar to other studies, the hot deformation process in this paper is a competition between work hardening and dynamic softening.^[25] This process can be divided into four stages: work hardening, the stable stage, softening, and the steady stage.^[26] These stages are clearly observed in Figure 2. Plastic deformation starts with the work hardening stage. Dislocation tangles, elongated, broken, or fibrous grains, along with the residual stress produced in the alloy are the main contributors to hot deformation work hardening. During the initial stage of deformation ($850 \text{ }^\circ\text{C}$, 0.001 s^{-1}), stress rises quickly because of the interaction of dislocations, and the residual stresses accumulate due to the work hardening rate being much higher than the dynamic softening rate. Figure 2 clearly indicates that low temperature and high strain rate cause work hardening to occur. For example,

the $550 \text{ }^\circ\text{C}$ curves still show work hardening at any strain. As deformation progresses, a stable stage occurs due to work hardening and dynamic recovery (DRV) being in equilibrium. In this stage, the stress increases slowly before eventually reaching a maximum value. However, dynamic recrystallization (DRX) is more pronounced at higher temperatures. For example, at $900 \text{ }^\circ\text{C}$, when softening effects dominate deformation, DRX occurs, and the flow stress decreases. This may be due to an increase in vacancy concentration with high temperatures and large deformations, which may have created more nucleation sites advantageous for dynamic recrystallization. At the last stage, the stress becomes steady because of the softening caused by DRX being in balance with work hardening.

The increased flow stress is primary due to the increase of internal dislocation density. Compared with the Cu–Zr alloy, the curves of the Cu–Zr–Y alloy have two trends during the hot deformation. Under some temperature conditions, such as $650 \text{ }^\circ\text{C}$,

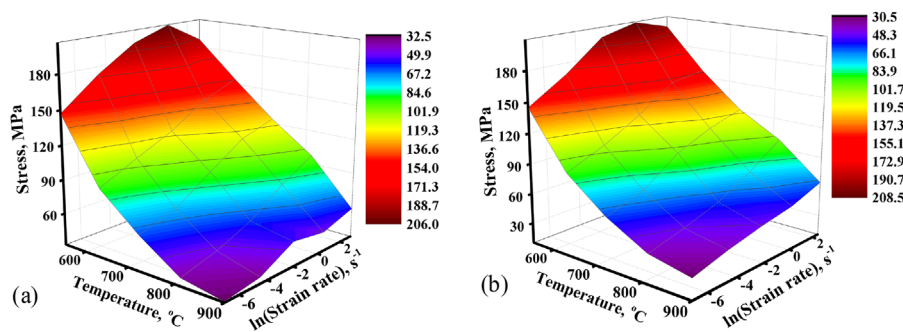


Figure 3. Peak stress dependence on temperature and strain rate for: a) Cu–Zr and b) Cu–Zr–Y alloys.

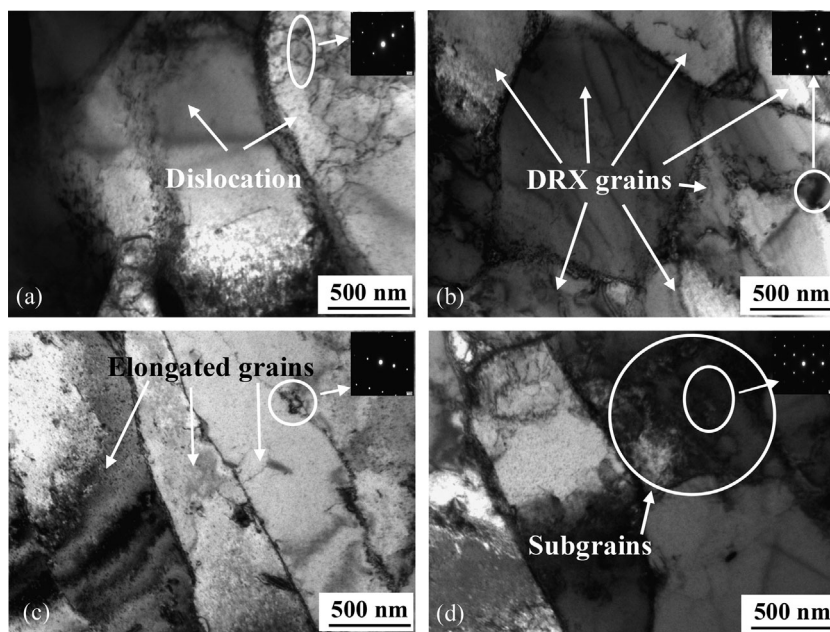


Figure 4. TEM micrographs of: a) Cu–Zr and b) Cu–Zr–Y alloys deformed at 900 °C and 0.01 s⁻¹ c) Cu–Zr; and d) Cu–Zr–Y alloys deformed at 650 °C and 0.01 s⁻¹.

low angle boundaries in Figure 4a and b. In addition, examination of Figure 4a and b immediately reveals that the grain size in Figure 4a is larger than in Figure 4b. This result indicates that the addition of Y improves grain refinement. Elongated grains separated by high angle boundaries are observed in Figure 4c, and many subgrains separated by low angle boundaries can be seen in Figure 4d. Therefore, it can be concluded that the addition of Y promotes DRX occurrence in the Cu–Zr–Y alloy, which is consistent with the results obtained by other researchers.^[27]

3.2. Y Effects on Hot Processing Maps and Microstructure

3.2.1. Hot Processing Map Principles

The processing map consists of superimposed instability and power dissipation plots. According to the processing map, the heating process of alloys can be optimized.^[28] It is built based on dynamic material model (DMM) principles.^[29] During hot deformation, materials are regarded as a structure of non-linear energy dissipation, assuming that the heat dissipation can be ignored. Input power (P) is transformed into plastic deformation (G) and microstructure evolution (J).^[30] The whole process can be represented as a function of stress (σ), strain (ϵ), and strain rate ($\dot{\epsilon}$):

$$P = \sigma \dot{\epsilon} = G + J = \int_0^{\epsilon} \sigma d\dot{\epsilon} + \int_0^{\sigma} \epsilon d\sigma \quad (1)$$

According to Equation 1, the relationship between G and J is:

$$m = \frac{dJ}{dG} = \frac{\dot{\epsilon} d\sigma}{\sigma d\dot{\epsilon}} = \frac{d \ln \sigma}{d \ln \dot{\epsilon}} \quad (2)$$

where m is the strain rate sensitivity exponent.

The relationship between the strain rate and the flow stress is shown in Figure 5. The straight-line “A” stands for the ideal linear dissipation process, and the curve “B” shows the nonlinear dissipation behavior, which is based on the theory of minimum energy.^[31] The former condition can make J reach the maximum value, $J_{\max} = \frac{1}{2} \sigma \dot{\epsilon}$. Under nonlinear conditions, power dissipation (η) is an important parameter for the determination of the extent of power dissipation by microstructural changes during hot deformation. It can be defined as^[30]:

$$\eta = J/J_{\max} = \frac{2m}{m+1} \times 100\% \quad (3)$$

A higher value of η indicates that the microstructure evolution occurs more efficiently. During hot deformation, DRX is generally a beneficial process, which can produce a stable flow.

The instability map is composed of both stable and unstable regions. It presents variations of the instability parameter $\xi(\dot{\epsilon})$ with different strain rates and temperatures. Prasad and Seshacharyulu^[32] proposed that $\xi(\dot{\epsilon})$ can be expressed as:

$$\xi(\dot{\epsilon}) = \frac{\partial \ln[m/(m+1)]}{\partial \ln \dot{\epsilon}} + m < 0 \quad (4)$$

3.2.2. Hot Processing Maps

Sivakesavam and Prasad^[33] have pointed out that processing maps obtained at any strain rate appear similar. Figure 6 shows

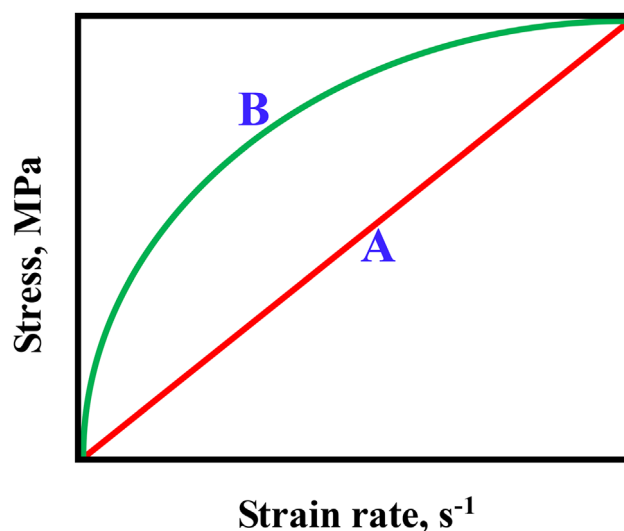


Figure 5. Relationship between the stress and the strain rate.

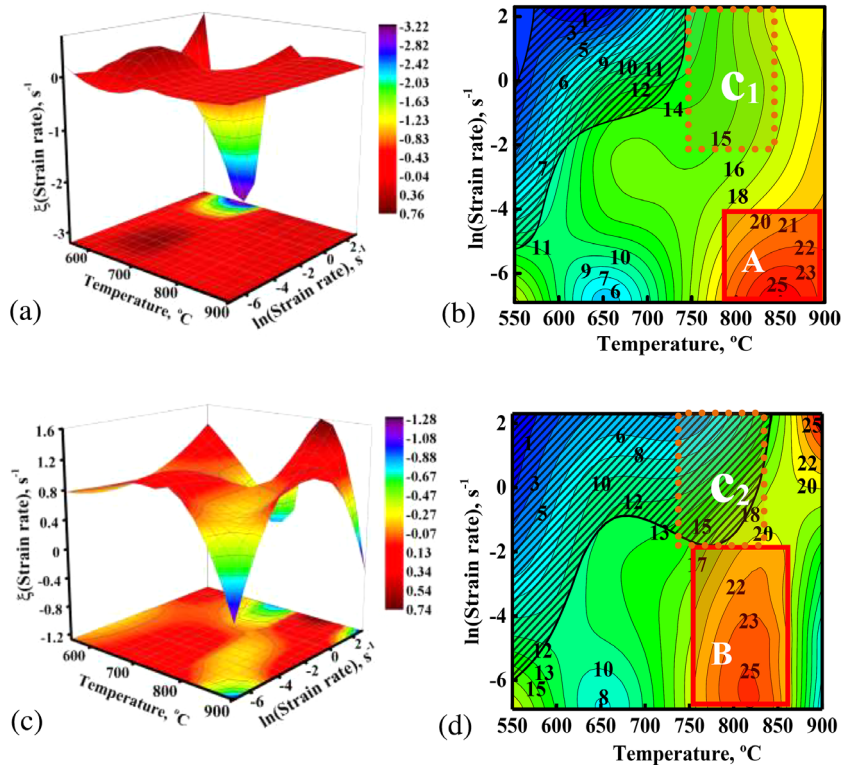


Figure 6. Instability zones and processing maps for: a), b) Cu–Zr and c), d) Cu–Zr–Y alloys at 0.4 strain.

the instability zones and processing maps for Cu–Zr and Cu–Zr–Y alloys at $\varepsilon = 0.4$. $\xi(\dot{\varepsilon})$ for the shaded regions in Figure 6b and d is negative, which indicates that hot deformation at these conditions is unsafe. Micro-cracks, or shear bands are observed in unstable regions, as seen in Figure 7f. During the hot deformation process, flow instability domains should be avoided.

As shown in Figure 6, the unstable regions for the two alloys exist in the area of high strain rate and low temperature with lower power dissipation. Safe zones are located at high temperature and low strain rate. By comparing Figure 6a and c, the instability region for the Cu–Zr–Y alloy is wider than for the Cu–Zr alloy. In the range of 740–840 °C, and 0.14–10 s⁻¹ (marked as region C), the $\xi(\dot{\varepsilon})$ parameter for the Cu–Zr alloy is positive, while for the Cu–Zr–Y alloy deformed in this domain, it is negative. This could be because the impurities pin the grain boundaries during hot deformation more than the precipitation process of the secondary phase. The impurities can impede the movement of dislocations and result in increased dislocation density. Therefore, the dislocation density in the Cu–Zr alloy is higher than in the Cu–Zr–Y alloy.^[34,35] In the 750–870 °C and 0.001–0.13 s⁻¹ ranges, the power dissipation for the Cu–Zr and Cu–Zr–Y alloys is 15–25% and 18–25%, respectively. The power dissipation of the Cu–Zr–Y alloy is higher than that of the Cu–Zr alloy, because the addition of Y can refine the crystalline structure and promote DRX. Comparing the processing maps for the two alloys at the 870–900 °C and 0.001–0.13 s⁻¹ ranges, the hot workability of the Cu–Zr alloy is better than that of the Cu–Zr–Y alloy. The main reason for this phenomenon is due

to the grains of the Cu–Zr–Y alloy being coarser than in the Cu–Zr. Flow stress-strain curves for 900 °C in Figure 2 point out that the addition of Y accelerates the rate of DRX and quickly completes the recrystallization. The crystal grains of the Cu–Zr–Y alloy have more time to grow and accompany the hot deformation.

The curves in Figure 6b and d represent efficiency of power dissipation, which increases with test temperature and decreasing strain rate. The highest value for the Cu–Zr and Cu–Zr–Y alloys is 25%. Based on this analysis, the optimal hot processing conditions for the Cu–Zr alloy are: 760–900 °C, 0.001–0.018 s⁻¹, and 18–25% efficiency of power dissipation. The addition of Y changed the best hot working parameters to: 750–870 °C, 0.001–0.13 s⁻¹, and the same 18–25% efficiency.

3.2.2. Y Effects on Microstructure Evolution

Microstructure changes of the Cu–Zr and Cu–Zr–Y alloys under different deformation conditions are shown in Figure 7. The corresponding processing map is obtained at 0.5 strain, which is similar to Figure 7. Flat and elongated grains are found in Figure 7a and d, indicating the microstructure of the alloy deformed at low temperature and high strain rate. The hot

deformation process is quick; therefore, the microstructure does not change significantly. In Figure 7a and d one can clearly see the original compressed microstructure. The average grain size of 149 μm for the Cu–Zr alloy is larger than 94 μm for the Cu–Zr–Y alloy because Y can effectively refine the grains. Figure 7g and h show that the optimal processing conditions for the Cu–Zr alloy are 800–900 °C with 0.001–10 s⁻¹, and for the Cu–Zr–Y alloy are 750–870 °C with 0.001–0.14 s⁻¹ and 850–900 °C with 0.36–10 s⁻¹. Comparing Figure 7b and e, it can be observed that DRX occurs, and is more noticeable for the Cu–Zr–Y alloy than for the Cu–Zr alloy. This shows that the addition of Y can promote DRX. The Cu–Zr alloy processing map areas at 870–90 °C and 0.001–0.005 s⁻¹ represent good workability, while the same areas for the Cu–Zr–Y alloy are unsafe. The main reason for this phenomenon are coarser grains. The same phenomenon can be observed in Figure 4b. The Cu–Zr–Y alloy, deformed at these conditions, easily cracks. Coarse 179 μm grains are found in the Cu–Zr–Y alloy, while the grains of the Cu–Zr alloy are quite small at 566 μm.

3.3. Constitutive Equations

Constitutive equations allow the prediction of the flow stress. The relationships between $\dot{\varepsilon} - \sigma$ and $\dot{\varepsilon} - T$ are^[36,37]:

$$\text{For lower stress : } \dot{\varepsilon} = A_1 \sigma^n \exp\left(-\frac{Q}{RT}\right) \quad (5)$$

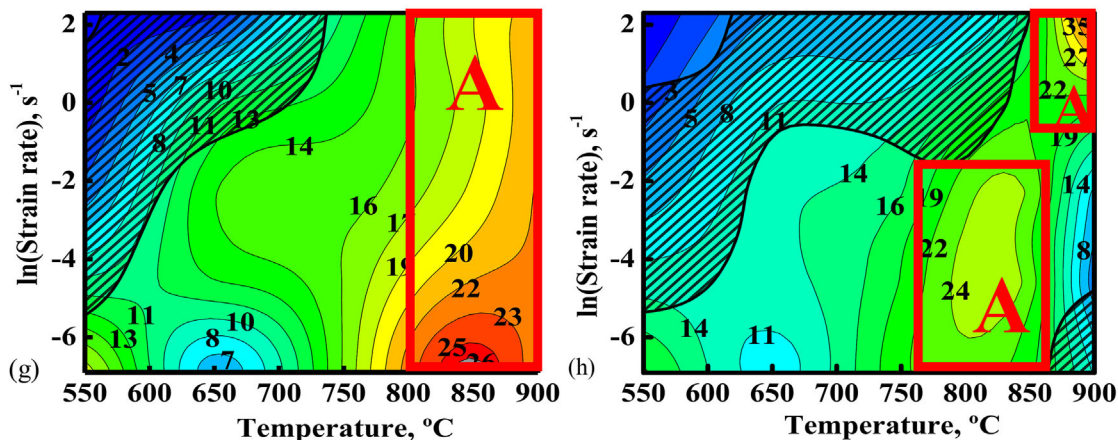
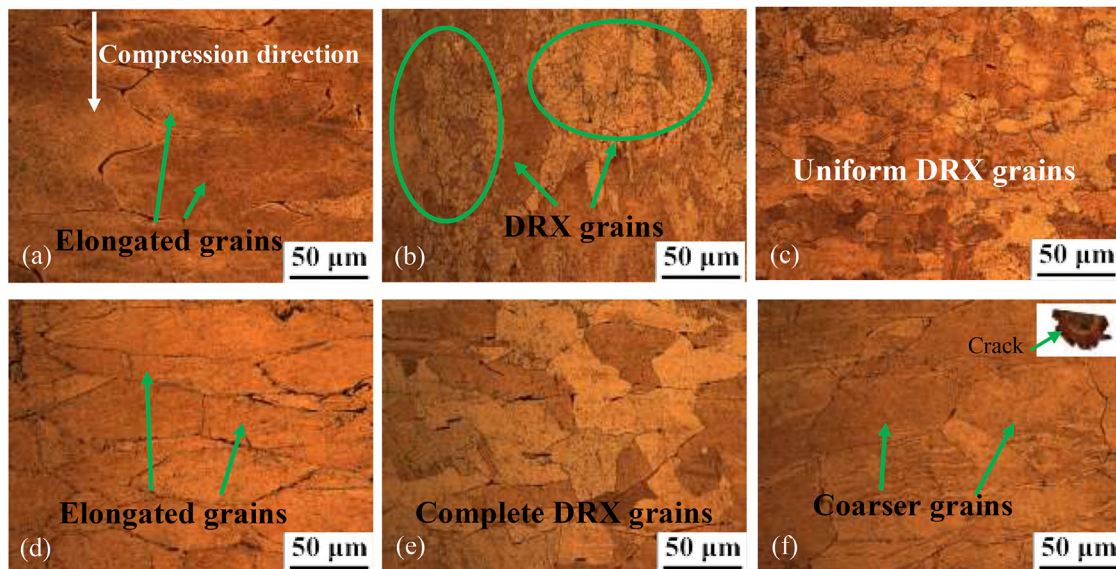


Figure 7. Optical micrographs of the samples deformed at different conditions: a) 550 °C and 1 s⁻¹ for Cu-Zr alloy; b) 850 °C, 0.01 s⁻¹ for Cu-Zr alloy; c) 900 °C, 0.1 s⁻¹ for Cu-Zr alloy; d) 550 °C and 1 s⁻¹ for Cu-Zr-Y alloy; e) 850 °C, 0.01 s⁻¹ for Cu-Zr-Y alloy; f) 900 °C, 0.001 s⁻¹ for Cu-Zr-Y alloy, and the processing maps for: g) Cu-Zr; and h) Cu-Zr-Y alloys at 0.5 strain.

$$\text{For higher stress : } \dot{\epsilon} = A_2 \exp(\beta\sigma) \exp\left(-\frac{Q}{RT}\right) \quad (6)$$

$$\text{For all : } \dot{\epsilon} = A[\sinh(\alpha\sigma)]^{n_1} \exp\left(-\frac{Q}{RT}\right) \quad (7)$$

Here, $\dot{\epsilon}$ is the strain rate in s⁻¹, σ is the flow stress in MPa, R is the universal gas constant, T is the thermodynamic temperature in K, Q is the activation energy for hot deformation in KJ · mol⁻¹, $\alpha = \beta/n_1$ is the stress parameter, and A , A_1 , A_2 , n , and n_1 are corresponding materials constants.

Shukla et al. have built the constitutive equation for the Cu-8Cr-4Nb alloy.^[38] In this paper, a Cu-Zr-Y alloy with 0.1 strain is used as an example to calculate material constants. Exponential $\dot{\epsilon} - T$ relationship was proposed by Sellars and McTegart.^[39] The

Zener-Hollomon Z parameter is introduced, such that the temperature (T) and the stress (σ) can be expressed as^[36]:

$$Z = \dot{\epsilon} \exp\left(\frac{Q}{RT}\right) = A[\sinh(\alpha\sigma)]^n \quad (8)$$

After some transformations, the following equations are obtained:

$$\ln \dot{\epsilon} = \ln A_1 - \frac{Q}{RT} + n \ln \sigma \quad (9)$$

$$\ln \dot{\epsilon} = \ln A_2 - \frac{Q}{RT} + \beta\sigma \quad (10)$$

$$\ln Z = \ln A + n_1 \ln[\sinh(\alpha\sigma)] \quad (11)$$

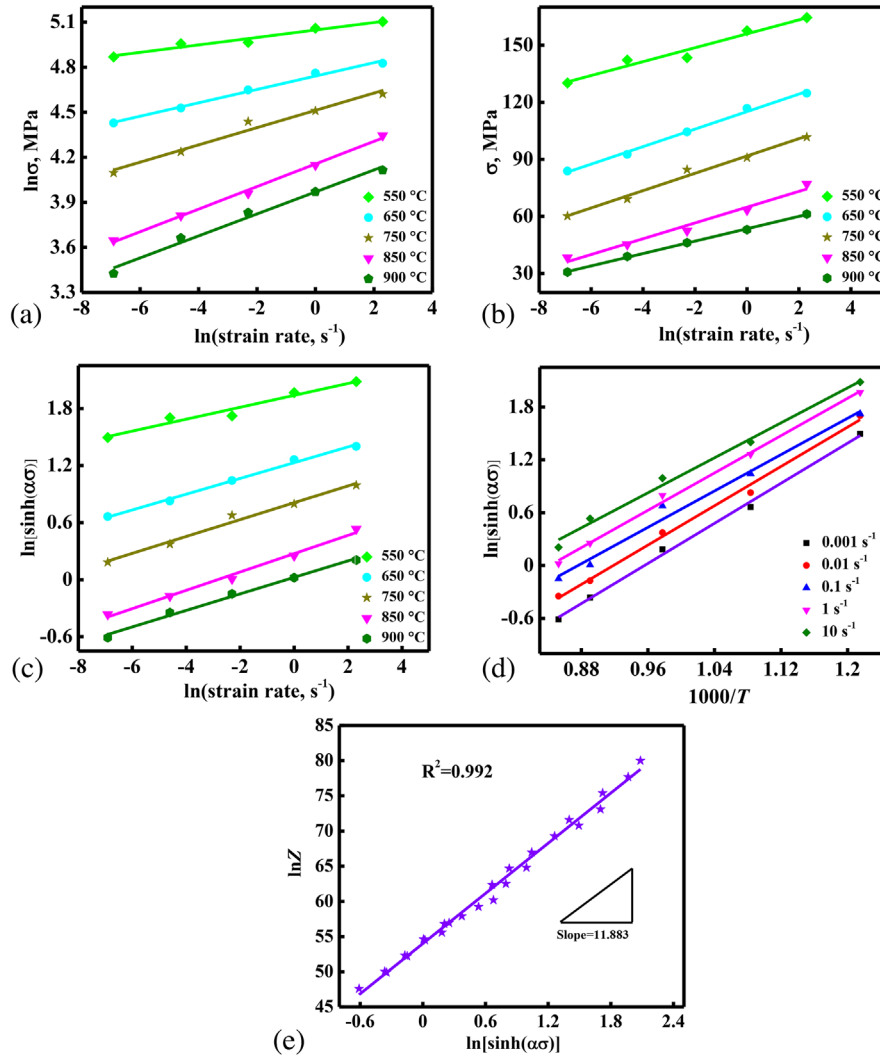


Figure 8. Relationships between: a) $\ln \dot{\epsilon}$ and $\ln \sigma$; b) $\ln \dot{\epsilon}$ and σ ; c) $\ln \dot{\epsilon}$, and $\ln[\sinh(\alpha\sigma)]$; d) $1/T$; and $\ln[\sinh(\alpha\sigma)]$; e) $\ln[\sinh(\alpha\sigma)]$ and $\ln Z$ for the Cu-Zr-Y alloy.

The relationship of $\ln\text{-}\ln\sigma$ could be described with the scatter diagram in **Figure 8a**. By using regression analysis, the value of $1/n = 0.069$, was obtained by taking an average value of the slopes of three lower stress lines in **Figure 8a**, that is, $n = 14.564$. The same technique can be applied for calculating other parameters. Based on **Figure 8b**, $\beta = 0.261 \text{ MPa}^{-1}$, which is an average value of the slopes of the three higher stress lines, and $\alpha = \beta/n = 0.018 \text{ MPa}^{-1}$.

By taking the logarithm and differentiating, Equation 7 can be transformed into:

$$Q = R \frac{\partial \ln[\sinh(\alpha\sigma)]}{\partial (1/T)} \bigg|_{\dot{\epsilon}} \frac{\partial \ln \dot{\epsilon}}{\partial \ln[\sinh(\alpha\sigma)]} \bigg|_T = R n_1 S \quad (12)$$

To calculate the values of S and n_1 , scatter diagrams of $\ln \dot{\epsilon}$ and $\ln[\sinh(\alpha\sigma)]$, and T^{-1} and $\ln[\sinh(\alpha\sigma)]$ are shown in **Figure 8c** and **d**, respectively. The corresponding average value of the five slopes in **Figure 8** are $S = 11.974$ and $n_1 = 5.34$. Thus, the activation energy $Q = R n_1 S = 531.607 \text{ kJ mol}^{-1}$.

Figure 8e shows a linear relationship for $\ln[\sinh(\alpha\sigma)]\text{-}\ln Z$. The slope and the intercept correspond to the values of $n_1 = 11.88$ and $\ln A = 54$, respectively. Therefore, the constitutive equations for the Cu-Zr and Cu-Zr-Y alloys, with strain of 0.1, are determined as:

For Cu-Zr alloy : $\dot{\epsilon} = 5.777$
 $\times 10^{25} [\sinh(0.014\sigma)]^{13.873} \exp\left(-\frac{532696}{8.314T}\right) \quad (13)$

For Cu-Zr-Y alloy : $\dot{\epsilon} = 2.844$
 $\times 10^{23} [\sinh(0.014\sigma)]^{11.883} \exp\left(-\frac{531607}{8.314T}\right) \quad (14)$

3.4. Constitutive Equation Verification

Many researchers have pointed out that strain has a profound effect on material constants.^[40,41] Thus, strain compensation is

Table 2. The 5th-order polynomial fitting results for $\ln A$, n , Q , and α .

	$\ln A$		n		Q		α	
	Cu-Zr	Cu-Zr-Y	Cu-Zr	Cu-Zr-Y	Cu-Zr	Cu-Zr-Y	Cu-Zr	Cu-Zr-Y
a_0	49.7	68.8	24.3	84.3	234.5	792.6	0.016	0.016
a_1	209.9	-276.4	-169.9	-365.3	5609.9	-4497.6	-0.017	-0.046
a_2	-1649.9	1628.2	857.4	1781.1	-35635.6	23924.1	-0.002	0.243
a_3	4415.1	-4053.3	-2141.4	-3737.7	92712.3	-56132.6	0.133	-0.613
a_4	-5220.1	4597.2	2528.3	3442.4	-110100.9	60216.9	-0.247	0.722
a_5	2344.2	-1945.4	-1127.1	-1092.9	49643.9	-24029.1	0.14	-0.32

crucial for accurate flow stress predictions. In this paper, strain compensation is taken into account to construct a more accurate constitutive equation. The values of four material constants are computed at different strains ranging from 0.1 to 0.7. Equation 15 shows the relationships between the strain and the material constants, where C represents material constants, while $\ln A$, n , Q , and α represent the fitting coefficients. The 5th-order polynomial fitting results for the two alloys are listed in **Table 2**.

$$C = a_0 + a_1\varepsilon + a_2\varepsilon^2 + a_3\varepsilon^3 + a_4\varepsilon^4 + a_5\varepsilon^5 \quad (15)$$

Based on Equation 8, the prediction of the flow stress can be expressed as a function of the Zener–Hollomon parameter:

$$\sigma = \frac{1}{\alpha} \ln \left\{ \left(\frac{Z}{A} \right)^{1/n} + \left[\left(\frac{Z}{A} \right)^{2/n} + 1 \right]^{1/2} \right\} \quad (16)$$

Based on the material constants, the flow stress can be predicted with Equation 16. To assess the accuracy for the established model, results of experimental stress and predicted flow stress are shown in **Figure 9**. The correlation coefficients for the Cu-Zr and Cu-Zr-Y alloys, mean squared errors, and an average relative error are $R=0.956$, 0.969 , $RMSE=10.75$, 9.84 , and $AARE=7.27$, 10.81% , respectively.

The following equations were used to calculate these parameters:

$$R = \frac{\sum_{i=1}^N (\sigma_e^i - \bar{\sigma}_e) (\sigma_p^i - \bar{\sigma}_p)}{\sqrt{\sum_{i=1}^N (\sigma_e^i - \bar{\sigma}_e)^2} \sqrt{\sum_{i=1}^N (\sigma_p^i - \bar{\sigma}_p)^2}} \quad (17)$$

$$RMSE = \sqrt{\frac{1}{N} \sum_{i=1}^N (\sigma_e^i - \sigma_p^i)^2} \quad (18)$$

$$AARE(\%) = \sum_{i=1}^N \frac{1}{N} \left| \frac{\sigma_e^i - \sigma_p^i}{\sigma_e^i} \right| \times 100 \quad (19)$$

Here, σ_e is the experimental stress in MPa, σ_p is the predicted stress in MPa, $\bar{\sigma}_e$ and $\bar{\sigma}_p$ are their respective averages, and N is the number of experimental data points. These results show that the obtained constitutive equation accurately predicts the flow stress.

3.5. Discussion

It is well known that hot deformation of alloys is a thermally activated process. The activation energy is an important physical parameter related to the degree of difficulty of plastic

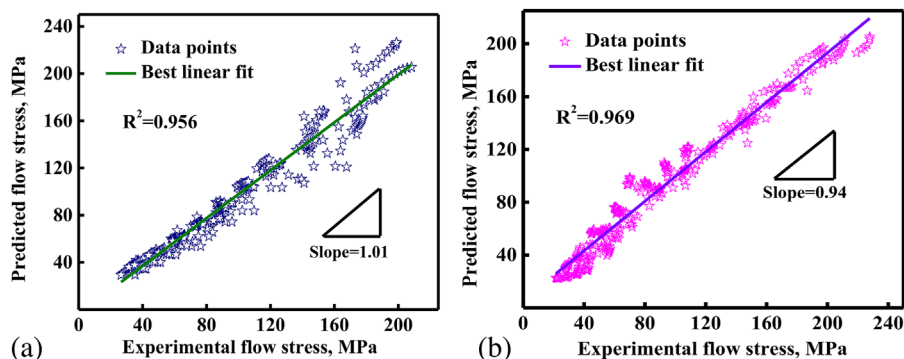


Figure 9. Correlation between predicted and experimental stress values for: a) Cu-Zr and b) Cu-Zr-Y alloys.

deformation.^[42] Heat can promote atomic motion and dislocation climb. These changes require activation energy, which is related to the alloy chemistry, strain, deformation temperature, strain rate, and grain size. During the whole hot deformation process, dislocations are produced by plastic deformation. Figure 10a shows how thermal deformation activation energy (Q) changes with strain. It can be clearly seen that the Cu–Zr–Y alloy has higher Q values than the Cu–Zr alloy at larger strains. This may be caused by a sharp dislocation density increase in the Cu–Zr alloy during the initial plastic deformation stage.^[16] Furthermore, the addition of Y reduces impurities compared to the Cu–Zr alloy, due to the element's high free radical chemical reactivity. The effect of impurity pinning keeps dislocations from sliding, so more energy is needed for dislocations movement. Thus, the thermal activation energy is higher without the Y addition. At a higher deformation temperature, a large number of precipitates occurs and their size becomes larger in the Cu–Zr–Y alloy. Furthermore, the addition of Y enlarges the stacking fault width, which increases the activation energy of dislocation slip.^[20,21] Thus, the dislocation density in the Cu–Zr–Y alloy is higher than in the Cu–Zr alloy, and the corresponding

thermal activation energy is also higher. This indicates that DRX occurs easier in the Cu–Zr–Y alloy compared to the Cu–Zr.

Power dissipation η is a parameter to characterize the energy of microstructure evolution. A higher power dissipation value means excellent workability during hot deformation. Figure 10b shows the comparison of peak efficiency of power dissipation η at seven strains ranging from 0.1 to 0.7 for both the Cu–Zr and Cu–Zr–Y alloys. Figure 10 shows that power dissipation η is strongly dependent on the strain rate and temperature. In Figure 5 and 6, η has a high value under high temperature and low strain rate and a low value at low temperature and high strain rate. This is due to the higher temperature providing more energy for microstructure evolution. At a lower strain rate, the alloys have ample time for microstructure evolution. According to Figure 10b, it can be seen that the Cu–Zr–Y alloy has higher efficiency of power dissipation than the Cu–Zr alloy, which means that the Cu–Zr–Y alloy has better workability than the Cu–Zr alloy during the hot deformation. Based on the analysis of Figure 7a–f, the Cu–Zr–Y alloy develops a fine uniform grain size earlier than the Cu–Zr alloy. Therefore, it can be concluded that the addition of a small amount of Y can promote microstructure evolution.

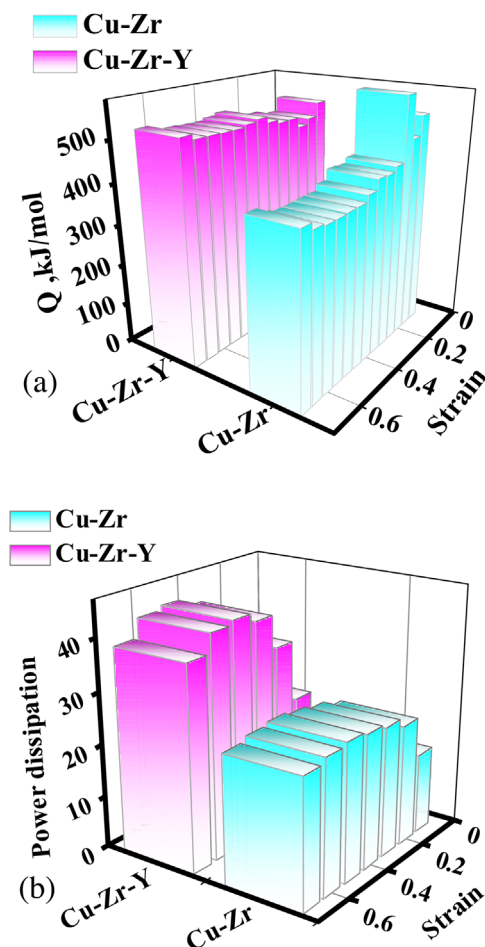


Figure 10. a) Thermal deformation activation energy Q and b) the peak efficiency of power dissipation η at different strain for the Cu–Zr and Cu–Zr–Y alloys.

4. Conclusions

Hot deformation behavior of the Cu–Zr and Cu–Zr–Y alloys was studied by using a thermo-mechanical simulator under diverse deformation conditions. According to the experimental results, the following conclusions are drawn:

- 1) During hot deformation, the flow stress of the Cu–Zr and Cu–Zr–Y alloys is sensitive to temperature and strain rate. Flow stress can be increased by deformation temperature and reduced by the strain rate.
- 2) Processing maps of the Cu–Zr and Cu–Zr–Y alloys were established and optimal deformation conditions were determined. Optimal deformation domains for the Cu–Zr alloy are 800–900 °C and 0.001–10 s^{−1}. Domains for the Cu–Zr–Y alloy are 750–870 °C, 0.001–0.14 s^{−1}, and 850–900 °C, 0.36–10 s^{−1}.
- 3) The addition of Y can refine the grains and promote DRX. The activation energy Q can be increased with the addition of a small amount of Y, which also slightly decreases the flow stress.
- 4) Under a given strain of 0.1, according to regression analysis of the stress–strain data, the activation energy of the deformed Cu–Zr and Cu–Zr–Y alloys was computed as 532.696 and 531.607 kJ mol^{−1}, respectively. New constitutive equations for the two alloys can be expressed as:

$$\text{For Cu–Zr alloy : } \dot{\epsilon} = 5.777 \times 10^{25} [\sinh(0.014\sigma)]^{13.873} \exp\left(-\frac{532696}{8.314T}\right)$$

$$\text{For Cu–Zr–Y alloy : } \dot{\epsilon} = 2.844 \times 10^{23} [\sinh(0.014\sigma)]^{11.883} \exp\left(-\frac{531607}{8.314T}\right)$$

5) The constitutive equations were verified for the Cu–Zr and Cu–Zr–Y alloys, and the corresponding values were found: $R = 0.956$, 0.969 , $RMSE = 10.75$, 9.84 , and $AARE = 7.27$, 10.81% , respectively.

Acknowledgements

This work was supported by the National Natural Science Foundation of China (51101052) and the National Science Foundation (IRES 1358088).

Conflict of Interest

The authors declare no conflict of interest.

Keywords

Y, Hot deformation, Cu–Zr and Cu–Zr–Y alloys, Processing map, Constitutive equation

Received: March 6, 2017

Revised: July 21, 2017

Published online: August 14, 2017

- [1] H. Zhang, H. Zhang, L. Li, *J. Mater. Process. Technol.* **2009**, *209*, 2892.
- [2] S. G. Mu, F. A. Guo, Y. Q. Tang, X. M. Cao, M. T. Tang, *Mater. Sci. Eng. A* **2008**, *475*, 235.
- [3] Q. Lei, Z. Li, M. P. Wang, L. Zhang, Z. Xiao, Y. L. Jia, *Mater. Sci. Eng. A* **2010**, *527*, 6728.
- [4] S. Higashijima, S. Sakurai, A. Sakasai, *J. Nucl. Mater.* **2011**, *417*, 912.
- [5] A. Chbihi, X. Sauvage, D. Blavette, *Acta Mater.* **2012**, *60*, 4575.
- [6] Y. Q. Long, P. Liu, Y. Liu, W. M. Zhang, J. S. Pan, *Mater. Lett.* **2008**, *62*, 3039.
- [7] S. J. Zhang, R. G. Li, H. J. Kang, Z. M. Chen, W. Wang, C. L. Zou, T. J. Li, T. M. Wang, *Mater. Sci. Eng. A* **2017**, *680*, 108.
- [8] N. Takata, S. H. Lee, N. Tsuji, *Mater. Lett.* **2009**, *63*, 1757.
- [9] I. S. Batra, G. K. Dey, U. G. Kulkarni, S. Banerjee, *J. Nucl. Mater.* **2001**, *299*, 91.
- [10] Y. X. Ye, X. Y. Yang, J. Wang, X. H. Zhang, Z. L. Zhang, T. Sakai, *J. Alloys Compd.* **2014**, *615*, 249.
- [11] Y. Zhang, A. A. Volinsky, H. T. Tran, Z. Chai, P. Liu, B. H. Tian, Y. Liu, *Mater. Sci. Eng. A* **2016**, *650*, 248.
- [12] C. D. Xia, Y. L. Jia, W. Zhang, K. Zhang, Q. Y. Dong, G. Y. Xu, M. P. Wang, *Mater. Des.* **2012**, *39*, 404.
- [13] J. P. Tu, W. X. Qi, Y. Z. Yang, F. Liu, J. T. Zhang, G. Y. Gan, N. Y. Wang, X. B. Zhang, M. S. Liu, *Wear* **2001**, *249*, 1021.
- [14] A. Gaganov, J. Freudenberger, E. Botcharova, L. Schultz, *Mater. Sci. Eng. A* **2006**, *437*, 313.
- [15] R. Y. Wang, P. Liu, J. G. Lei, Y. Liu, B. X. Kang, B. H. Tian, *Hot Work. Technol.*, **2004**, *6*, 3.
- [16] N. Haque, A. Hughes, S. Lim, V. Chris, *Resources* **2014**, *3*, 614.
- [17] F. S. Yuan, H. Y. Zhong, P. Jin, J. T. Tian, *Technol. Eng.* **2010**, *4*, 19.
- [18] F. A. Mirza, D. L. Chen, D. J. Li, X. Q. Zeng, *Mater. Des.* **2013**, *46*, 411.
- [19] G. Carro, A. Munoz, M. A. Monge, B. Savoini, A. Galatanu, R. Pareja, *Fusion Eng. Des.* <https://doi.org/10.1016/j.fusengdes.2017.01.017>
- [20] L. K. Tan, Y. Li, S. C. Ng, L. Lu, *J. Alloys Compd.* **1998**, *278*, 201.
- [21] L. G. Han, Q. E. Meng, S. Ren, *J. Iron Steel Res. Int.* **1984**, *4*, 305.
- [22] Z. R. Pei, R. Li, *Comput. Mater. Sci.* **2017**, *133*, 1.
- [23] Y. Zhang, A. A. Volinsky, H. T. Tran, Z. Chai, P. Liu, B. H. Tian, *J. Mater. Eng. Perform.* **2015**, *24*, 3783.
- [24] Y. Zhang, B. H. Tian, A. A. Volinsky, X. H. Chen, H. L. Sun, Z. Chai, P. Liu, Y. Liu, *J. Mater. Res.* **2016**, *31*, 1275.
- [25] G. Kugler, R. Turk, *Acta Mater.* **2004**, *52*, 4659.
- [26] B. K. Raghunath, K. Raghukandan, R. Karthikeyan, K. Palanikumar, U. T. S. Pillai, R. A. Gandhi, *J. Alloys Compd.* **2011**, *509*, 4992.
- [27] Y. Zhang, Z. Chai, A. A. Volinsky, B. H. Tian, H. L. Sun, P. Liu, Y. Liu, *Mater. Sci. Eng. A* **2016**, *662*, 320.
- [28] S. Anbuselvan, S. Ramanathan, *Mater. Des.* **2010**, *31*, 2319.
- [29] Y. V. R. K. Prasad, H. L. Gegel, S. M. Doraivelu, J. C. Malas, J. T. Morgan, K. A. Lark, D. R. Barker, *Metall. Trans. A* **1984**, *15*, 1883.
- [30] H. Zhou, Q. D. Wang, B. Ye, W. Guo, *Mater. Sci. Eng. A* **2013**, *576*, 101.
- [31] H. L. Gegel, *Computer Simulation in Materials Science*. Materials Park, Ohio, USA **1986**, p. 291.
- [32] Y. Prasad, T. Seshacharyulu, *Int. Mater. Rev.* **1998**, *43*, 243.
- [33] O. Sivakesavam, Y. Prasad, *Mater. Sci. Eng. A* **2003**, *362*, 118.
- [34] P. J. Apps, J. R. Bowen, P. B. Prangnell, *Acta Mater.* **2003**, *51*, 2811.
- [35] M. R. Shankar, S. Chandrasekar, A. H. King, W. D. Compton, *Acta Mater.* **2005**, *53*, 4781.
- [36] C. Zener, *J. H. Hollomon. J. Appl. Phys.* **1944**, *15*, 22.
- [37] Y. C. Lin, X. M. Chen, *Mater. Des.* **2011**, *32*, 1733.
- [38] A. K. Shukla, S. V. S. N. Murty, S. C. Sharma, K. Mondal, *Mater. Des.* **2015**, *75*, 57.
- [39] C. M. Sellars, W. J. McTegart, *Acta Metall.* **1966**, *14*, 1136.
- [40] S. Mandal, V. Rakesh, P. V. Sivaprasad, S. Venugopal, K. V. Kasiviswanathan, *Mater. Sci. Eng. A* **2009**, *500*, 114.
- [41] D. Samantaray, S. Mandal, A. K. Bhaduri, *Mater. Des.* **2010**, *31*, 981.
- [42] H. C. Liao, Y. N. Wu, K. X. Zhou, J. Yang, *Mater. Des.* **2015**, *65*, 1091.